



Article

Magnetic Isotropy/Anisotropy in Layered Metal Phosphorous Trichalcogenide MPS_3 (M = Mn, Fe) Single Crystals

Zia ur Rehman ^{1,2,†}, Zahir Muhammad ^{1,†}, Oyawale Adetunji Moses ¹, Wen Zhu ¹,
Chuanqiang Wu ¹, Qun He ¹, Muhammad Habib ¹ and Li Song ^{1,*} 

¹ National Synchrotron Radiation Laboratory, CAS Center for Excellence in Nanoscience, University of Science and Technology of China, Hefei 230029, China; zurehman@mail.ustc.edu.cn (Z.u.R.); zahir@mail.ustc.edu.cn (Z.M.); oyawaletj@mail.ustc.edu.cn (O.A.M.); sa2016@mail.ustc.edu.cn (W.Z.); wucq@mail.ustc.edu.cn (C.W.); hqun@mail.ustc.edu.cn (Q.H.); mhabib@mail.ustc.edu.cn (M.H.)

² Department of Applied Physics, University of Karachi, Karachi-75270, Pakistan

* Correspondence: song2012@ustc.edu.cn; Tel.: +86-551-6360-2102

† These two authors contributed equally in this work.

Received: 12 May 2018; Accepted: 8 June 2018; Published: 11 June 2018



Abstract: Despite the fact that two-dimensional layered magnetic materials hold immense potential applications in the field of spintronic devices, tunable magnetism is still a challenge due to the lack of controllable synthesis. Herein, high-quality single crystals MPS_3 (M= Mn, Fe) of millimeter size were synthesized through the chemical vapor transport method. After systemic structural characterizations, magnetic properties were studied on the bulk MPS_3 layers through experiments, along with first principle theoretical calculations. The susceptibilities as well as the EPR results evidently revealed unique isotropic and anisotropic behavior in $MnPS_3$ and $FePS_3$ crystals, respectively. It is worth noting that both of these materials show antiferromagnetic states at measured temperatures. The estimated antiferromagnetic transition temperature is 78 K for bulk $MnPS_3$ and 123 K for $FePS_3$ crystals. The spin polarized density functional theory calculations confirmed that the band gap of the antiferromagnetic states could be generated owing to asymmetric response all over the energy range. The ferromagnetic state in $MnPS_3$ and $FePS_3$ is less stable as compared to the antiferromagnetic state, resulting in antiferromagnetic behavior. Additionally, frequency-dependent dielectric functions for parallel and perpendicular electric field component vectors, along with the absorption properties of MPS_3 , are thoroughly investigated.

Keywords: layered material; bulk single crystal; isotropy; anisotropy; chemical vapor transport (CVT); density-functional theory (DFT)

1. Introduction

Magnetism has been proven to be widely helpful in the understanding of the quantum nature of materials. Although 2D transition metal dichalcogenides (TMDs) have been the center of attention in the recent era, transition metal chalcogenophosphates (TMCs) with general formula of MPX_3 (M = Mn, Fe, Ni, Co and X = S, Se) have also proven to be unique materials with their low-dimensional magnetic properties. These MPX_3 have secured renewed interest owing to their importance, not only for fundamental research, but also as potential candidates for numerous technological applications [1–10]. They belong to one of the few layered systems having 2D lattice for both magnetic and crystallographic systems. These materials possess two spin channels, one conducting and the other insulating. This family of materials is considered to be the best suited for applications in spintronic [11,12]. Over the last few years, MPX_3 have gained attention because of their enormous potential as a material

for next generation electronics. In this regard, MnPS₃ has been the focus because of electron valley freedom coupled with antiferromagnetic order [13]. A minute amount of magnetic field leak makes these antiferromagnetic materials a well-suited choice for use in robust data storage applications [14,15]. In recent years, layered antiferromagnetic materials have been used to induce deterministic switching without an external magnetic field [16]. Additionally, the higher magnetic resonance frequency of antiferromagnetic materials, in comparison with ferromagnetic materials, has attracted their use in providing high-speed data processing [17].

MnPS₃ and FePS₃ belong to the same MPX₃ class of materials with isotropic and anisotropic magnetic susceptibilities, respectively [18]. Both MnPS₃ and FePS₃ are layered magnetic materials with weak Van der Waal forces separating the layers. The presence of the Van der Waal gap rules out the possibility of superexchange pathways as well as minimizes the possibility of direct exchange owing to metal-metal interlayer distance of ~6.5 Å and 6.4 Å in MnPS₃ and FePS₃, respectively. These materials can be exfoliated into a single layer [19] and possess a magnetic ground state, dependent on transition metal element [18].

MPX₃ materials have been mostly investigated for their intercalation properties [9]. These are wide bandgap, highly resistive semiconductors having bandgap of the order of 3 eV. Bandgaps for MnPS₃ and FePS₃ are approximately 2.4 and 1.5 eV, respectively. The adequate amount of bandgap makes these materials a suitable semiconductor for optoelectronic [20], optoelectronic material processing [6], while MnPS₃ has also been realized as a promising photocatalyst for water splitting [21]. MnPS₃ is optically transparent with a greenish color [22], while FePS₃ has a brownish appearance. More importantly, the magnetic character of MnPS₃ arises from Mn²⁺ having spin 5/2 that forms a honeycomb lattice in a, b plane. The weak Van der Waal interlayer coupling is attributed to S atoms, but the antiferromagnetic phase transition at 78 K points towards an interplane exchange that can be associated with some degree of metal-ligand covalency [23,24]. FePS₃ is a striking compound because of the fact that it exhibits stronger magnetic interactions between Fe²⁺ ions in comparison with Mn²⁺ as well as due to the reason that electronic structure of the Fe²⁺ ions demonstrate strong anisotropy [18,25]. The isotropic/anisotropic nature affects the frequency-dependent dielectric and absorption properties of MPS₃ as well. All these facts make these MPS₃ ideal candidates for 2D magnetic as well as optoelectronic systems.

Herein, we report the chemical vapor transport (CVT) synthesis of highly crystalline, millimeter-size MPS₃ (M = Mn, Fe) single crystals. Furthermore, the magnetic isotropic/anisotropic properties of bulk MPS₃ single crystals were tested using electron paramagnetic resonance (EPR) and vibrating sample magnetometer (VSM). Experimental results revealed the antiferromagnetic nature of these materials with MnPS₃ exhibiting isotropic whereas, FePS₃ showed highly anisotropic properties measured by magnetic susceptibilities. The magnetic and dielectric properties of these materials were confirmed using first principle spin polarized density-functional theory (DFT) calculations.

2. Experiments

The millimeter-sized MnPS₃ and FePS₃ single crystals were prepared using CVT method. The charge for MnPS₃ and FePS₃ was prepared by using a stoichiometric amount of Mn, P, S and Fe, P, S for MnPS₃ and FePS₃, respectively. Iodine was used as transport agent for this growth. The charge was kept in a 17-cm long silica tube, and was sealed under vacuum ($\approx 10^{-1}$ atm). The sealed ampoule was placed inside a two-zone furnace with a hot zone temperature of 650 °C and cold zone temperature of 600 °C for 7 days. The reaction yielded pale green colored single crystals and brownish single crystals at the low temperature end of ampoule for MnPS₃ and FePS₃, respectively.

The structural study of as-prepared samples was carried out by using X-ray diffraction (XRD) and high-resolution transmission electron by microscope (TEM); phonon spectrum was studied by using Raman Spectroscopy, chemical composition by using X-ray photoelectron spectroscopy (XPS), the morphology of the samples was investigated by using scanning electron microscope (SEM). The magnetic properties of these bulk crystal samples were studied by using electron paramagnetic

resonance (EPR), and physical properties measurement system (PPMS) through vibrating sample magnetometer (VSM).

3. Results and Discussions

Typical SEM images of as-obtained MnPS_3 and FePS_3 samples are shown in Figure 1a,b. It can be seen that both MnPS_3 and FePS_3 exhibit smooth surfaces with roughly hexagonal morphology. The SEM images also show a layered structure of MPS_3 . Inset Figure 1a,b depict millimeter size as grown single crystals of MnPS_3 and FePS_3 , respectively. Figure 1c,d represent the Raman spectra of MnPS_3 and FePS_3 recorded at room temperature using 532 nm laser excitation. For MnPS_3 , the Raman peaks at 114.3, 152.2, 245 and 568 cm^{-1} are identified as E_g vibrating mode, and 273.3, 283.1 and 580 cm^{-1} are recognized as A_{1g} mode [21]. In the case of FePS_3 , the Raman peaks at 97.3, 155.9, 224.1, 246.8 cm^{-1} are identified as E_g vibrating mode whereas, peaks at 279 and 379.2 cm^{-1} are referred to as A_{1g} mode [23].

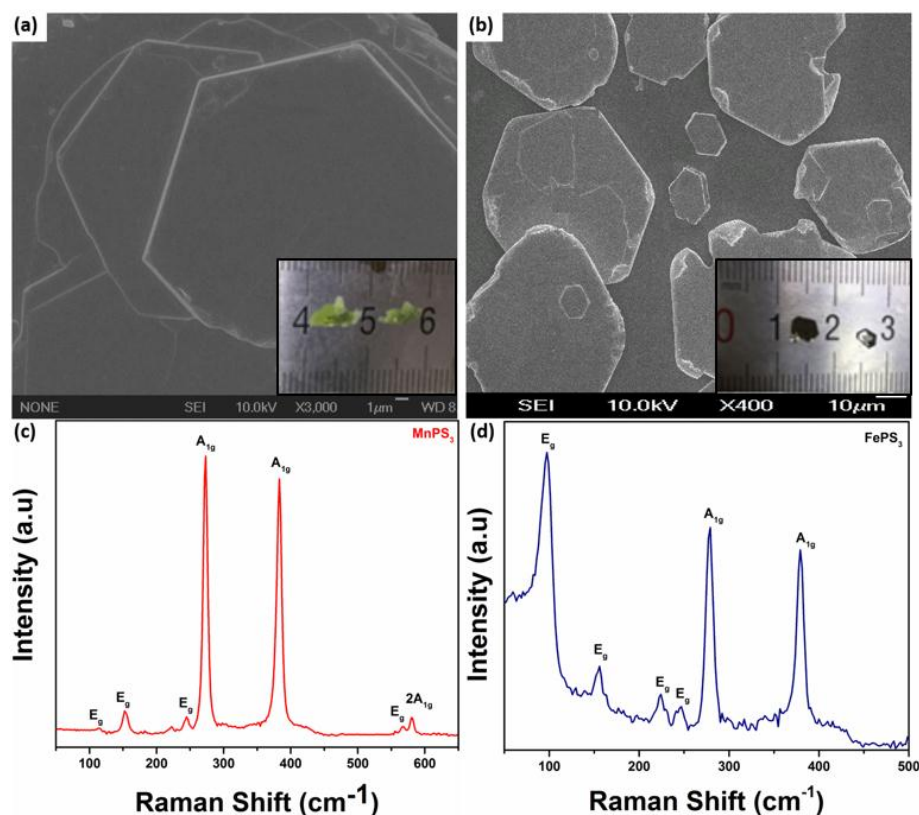


Figure 1. (a,b) Scanning electron microscope (SEM) images, inset shows millimeter sized as grown single crystals and (c,d) Raman spectra of as-obtained MnPS_3 and FePS_3 single crystals, respectively.

The X-ray diffraction data (XRD) of the samples were analyzed to study the crystal planes and crystallinity of MnPS_3 and FePS_3 single crystals. It is evident from Figure 2a,b that these results are well in accordance with the standard JPCDS cards belonging to (PDF#33-0903, PDF#30-0663) MnPS_3 and FePS_3 , respectively. The crystal lattice and phase identification revealed that both MnPS_3 and FePS_3 exhibit high-quality single crystals with major (001) and (002) peaks. The absence of any impurity peak suggests that these samples have pure phases. Inset in Figure 2a,b shows the crystallographic model of MnPS_3 and FePS_3 along (001) plane, respectively. Figure 2c,d displays the TEM images of MnPS_3 and FePS_3 , suggesting that both samples are highly crystalline with growth as single crystal. The d-spacing calculated from Figure 2c,d is estimated as 0.25 nm and 0.30 nm corresponding to (20 $\bar{2}$) and (20 $\bar{1}$)

planes in MnPS_3 , while 0.25 nm and 0.29 nm correspond to (131) and $(\bar{2}01)$ planes in monoclinic unit cell of FePS_3 .

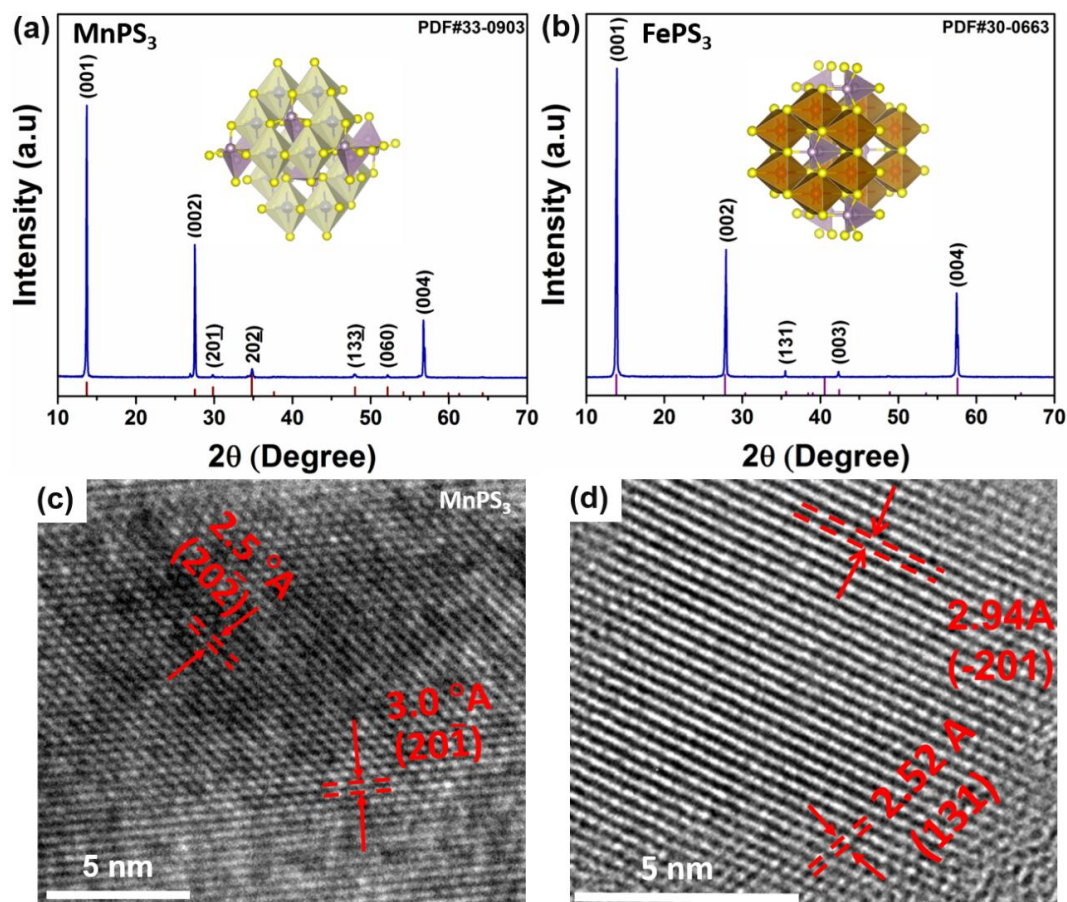


Figure 2. (a,b) X-ray diffraction patterns and (c,d) high resolution transmission electron by microscope (TEM) images for MnPS_3 and FePS_3 single crystals prepared by ball-milling and sonication process.

The chemical composition and bonding state of the samples were studied by using XPS analysis, as shown in Figure 3. The Mn 2p peaks of MnPS_3 detected at 652.8 and 641 eV can be assigned to $2p_{3/2}$ and $2p_{1/2}$, respectively. The S 2p, peaks identified at 162.75 and 163.9 eV can be assigned to $2p_{3/2}$ and $2p_{1/2}$. For P 2p, two peaks at 132.5 eV and 133.6 eV are assigned to $2p_{3/2}$ and $2p_{1/2}$. In case of FePS_3 , the Fe 2p peaks at 709 and 722 eV are assigned to $2p_{3/2}$ and $2p_{1/2}$. Both S 2p and P 2p peaks of FePS_3 show quite similar position and shape as those peaks for MnPS_3 . All these values are consistent with the previous reports [26,27].

Magnetic susceptibility indicates the magnetic properties of a material. It depicts the degree of magnetization of a material with respect to temperature at constant applied magnetic field. The magnetic susceptibility (χ) as a function of temperature for both MnPS_3 and FePS_3 crystals is represented in Figure 4a,b. The susceptibility plots of MnPS_3 and FePS_3 were examined through field cooling (FC) and zero field cooling (ZFC) curves. From the susceptibility plots, we can observe the isotropic behavior of MnPS_3 , while for FePS_3 a considerable anisotropic trend has been noticed. The susceptibilities of MnPS_3 and FePS_3 increase with decreasing temperature till at 120 K and 128 K, respectively. Beyond this point it shows rapid decrease, exhibiting a Curie like tail at lowest temperatures. Furthermore, the susceptibility is seen to follow the Curie-Weiss law at higher temperatures (inset Figure 4a,b), which is an identification feature of the antiferromagnetic nature of these materials [7]. It can be inferred from Figure 4a,b that Neel temperature for MnPS_3 and FePS_3 are 78 K and 123 K, while the corresponding Curie temperatures are found to be at 365 K and 324 K,

respectively. These values of Neel temperature and Curie temperature are well matched with the previous reports [28,29]. The broad maxima above Neel temperature is a result of short-range spin-spin correlation in typical magnetic systems. We can observe that magnetic susceptibility for FC is higher than ZFC throughout the observed range for both MnPS₃ and FePS₃. The increased Curie temperature beyond room temperature shows that these materials are favorable for spintronic applications.

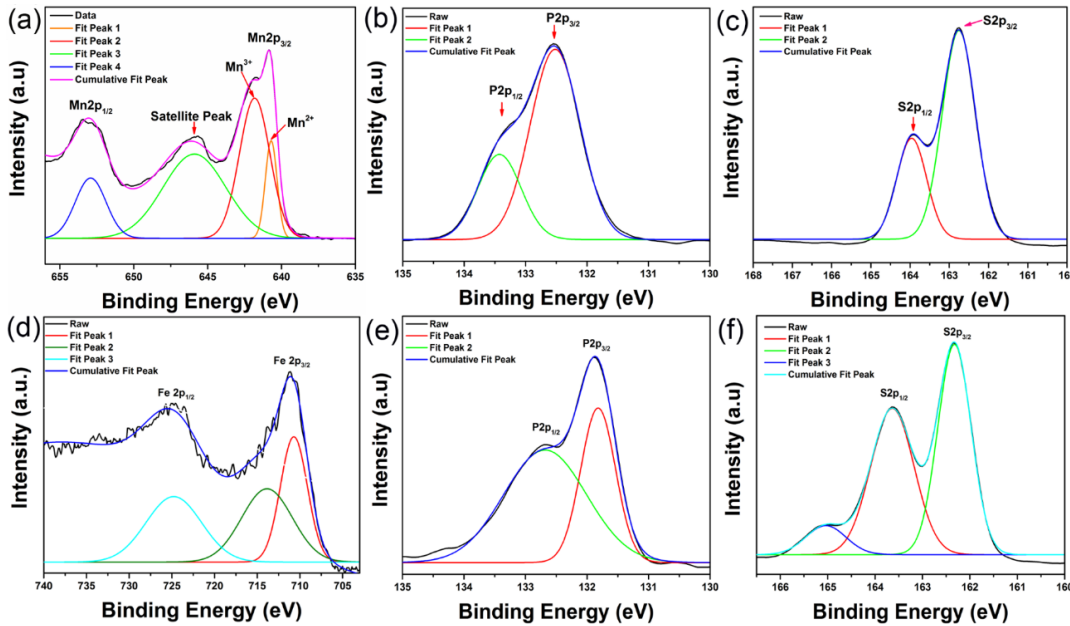


Figure 3. X-ray photoelectron microscopy of (a–c) MnPS₃ and (d–f) FePS₃ single crystals.

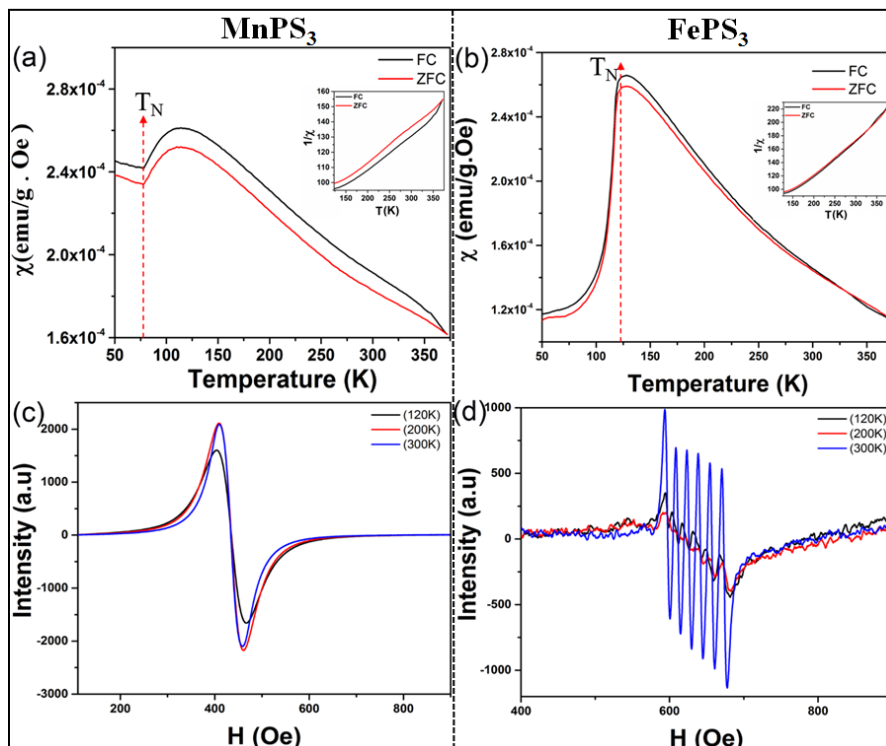


Figure 4. Magnetic susceptibility of (a) MnPS₃ and (b) FePS₃ single crystals with millimeter size. Electron paramagnetic resonance spectra of (c) bulk MnPS₃ and (d) FePS₃ single crystals.

The electron paramagnetic resonance (EPR) method was employed to study the quantum mechanical mixed spin states of both samples. The EPR signal typically originates from the surface of electrons, which increases by the exposures of some metals. The EPR spectra of the samples were measured at 120 K, 200 K and 300 K at constant frequency of 9 GHz. Figure 4c,d depicts the EPR spectra of MnPS₃ and FePS₃ with unpaired electrons. For MnPS₃, the EPR spectra is isotropic, with the magnetic signals containing a single narrow resonance peak (Figure 4c). On the other hand, EPR spectra for FePS₃ is highly anisotropic with multiple magnetic resonance peaks (Figure 4d). The magnetic resonance peaks for MnPS₃ occurs at 404.1, 410 and 410.33 mT, while multiple resonance peaks were observed for FePS₃ at all measured temperatures as described in Table 1. The strong signals at 300K for FePS₃ can be attributed to the shortening of relaxation time with temperature in anisotropic materials [30,31]. Details for the position of six resonance peaks observed for FePS₃ along with their corresponding values of g-factor is given in Table 1.

Table 1. Resonance peak position and value of g-factor for bulk FePS₃ single crystals.

Temperature	Value of g-Factor (Resonance Peak Position, mT)					
	Peak 1	Peak 2	Peak 3	Peak 4	Peak 5	Peak 6
300 K	1.080 (593.62)	1.057 (608.36)	1.032 (623.11)	1.007 (638.5)	0.983 (653.9)	0.9589 (670.6)
200 K	1.088 (590.9)	1.062 (605.0)	1.036 (621.0)	1.007 (638.5)	0.986 (651.85)	0.9592 (670.6)
120 K	1.082 (594.27)	1.066 (602.95)	1.043 (616.39)	1.018 (631.13)	0.990 (649.14)	0.9646 (666.59)

The magnetic coupling factor or g-factor “ g_{eff} ” was computed from EPR spectra using the following relationship [32]:

$$g_{\text{eff}} \cong \frac{h\nu}{\mu_B H_{\text{center}}} \quad (1)$$

where “ ν ” is the frequency, “ h ” is Planck constant, “ μ_B ” indicating Bohr magneton and H_{center} is the resonance magnetic field. The calculated values of g_{eff} are found to be 1.5921, 1.5684, and 1.5679 at 120, 200 and 300 K for MnPS₃.

Anisotropy of magnetization originates from the anisotropy of the particles themselves in the form of shape or crystalline anisotropy and degree of alignment. The crystalline anisotropy relies on lattice forces and subsequent magnetization along an easy axis. EPR spectrum intensity is affected by number, position and nature of magnetic ions as well as the spin environment e.g., electron spin exchange with identical and non-identical atoms or molecules or with the spin of unpaired electrons of neighboring molecules. Additionally, in case of single crystals having equal orientations, it is expected that one defect will exist in all orientations with equal probability. For a low symmetry g-tensor and at an arbitrary direction of magnetic field, different effective values of g-factors are possible for the different orientations of the defect that can give rise to different magnetic field positions of EPR lines [33]. In fact, isotropy and anisotropy also affect the dielectric and absorption properties of materials. Isotropic materials display uniform dielectric functions along different directions, whereas anisotropic materials possess direction-dependent dielectric properties. In order to further understand the effect of isotropic and anisotropic behavior, spin-polarized first-principle density functional theory (DFT) calculations were performed to describe the magnetic response of MPS₃ (M = Fe, Mn). The computations were carried out by using DFT through Vienna ab initio simulation package (VASP) [34]. A projector augmented wave (PAW) method [35,36] was used to characterize the ion-electron interface and the generalized gradient approximation (GGA) was stated by the PBE functional [37,38]. The plane wave cutoff energy was set to 500 eV with energy precision of 10^{-5} eV. The force criteria on each atom was less than 10^{-2} eV/Å. The Brillouin zone Γ -centered was sampled with a $12 \times 12 \times 1$ Monkhorst–Pack of k-points grid for geometry optimization, while the static electronic calculation $8 \times 8 \times 1$ and self-consistent calculations of the MPS₃ (M = Mn, Fe) system were made. Unit cells were considered for these calculations. To obtain electronic and magnetic results, we employed a partition by hybrid HSE06 functional [38,39] with an accurate Fock exchange and typically achieved much better results than

the DFT and DFT+U methods [40]. A single unit cell with lattice parameters of MnPS_3 ($a = 6.076 \text{ \AA}$, $b = 10.524 \text{ \AA}$ and $c = 6.796 \text{ \AA}$) and FePS_3 ($a = 5.949 \text{ \AA}$, $b = 10.288 \text{ \AA}$ and $c = 6.72 \text{ \AA}$) from the experimental data has been used for calculations.

According to our magnetic energy calculations that are listed in Table 2, the ferromagnetic state in both cases is less stable as compared to the antiferromagnetic state, with an energy difference of about 0.601 eV for MnPS_3 , while for FePS_3 the difference in energies is around 1.02 eV. Total energy calculations clearly defined that the room temperature antiferromagnetic (RTAFM) state is in the ground state of MPS_3 ($M = \text{Fe, Mn}$).

Similarly, the density of states (DOS) calculations in Figure 5 show the asymmetry between the spin-up and spin-down state of MPS_3 ($M = \text{Fe, Mn}$). Figure 5a,b shows the evidence of magnetism for both MnPS_3 and FePS_3 layers with asymmetric density states in different energy levels. It can be seen that the electronic density of MnPS_3 mainly stems from $M'd$, $P'p$ and $S'p$ states. Particularly, strong hybridization of $M'n'd$, $P'p$ and $S'p$ states is found between -7 eV and -1 eV , while strong $P'p$ and weak $M'n'd$, and $S'p$ was witnessed between 4 eV and 5 eV . However, near the Fermi level, strong $S'p$ and weak $M'n'd$ states exist, as shown in Figure 5a. Similarly for FePS_3 , $\text{Fe}'d$, $P'p$ and $S'p$ states exist between -7 eV and -2 eV , and strong $P'p$ and weak $M'n'd$, and $S'p$ appear between 4 eV and 6 eV . Likewise, strong $S'p$ and a weak $\text{Fe}'d$ states exist near the Fermi level, as shown in Figure 5b. All these states (spin-up and spin-down) are asymmetric and contribute to the magnetic isotropic/anisotropic trend throughout the energy range. The d -orbitals of Mn and Fe have the most obvious contribution of spinpolarization, which mainly contributes towards the magnetism of MPS_3 .

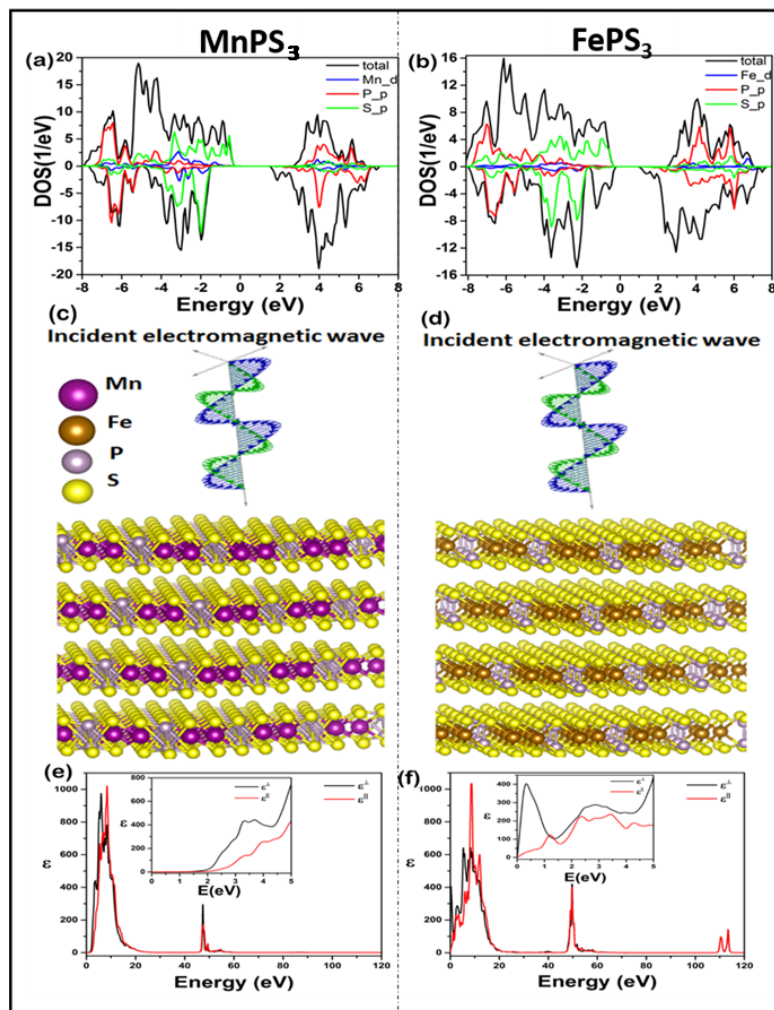


Figure 5. (a,b) Projected density of states of MnPS_3 and FePS_3 (c,d) structure of MnPS_3 and FePS_3 under incident electromagnetic wave (e,f) calculated dielectric function for MnPS_3 and FePS_3 , respectively.

The frequency-dependent dielectric functions have been calculated using parallel and perpendicular electric field component vectors along the c-axis, as shown in Figure 5c,d. The frequency-dependent dielectric functions in Figure 5e,f show a strong isotropic and anisotropic behavior in lower and higher energy ranges for MnPS₃ and FePS₃, respectively. It was found that MnPS₃ shows strong isotropic behavior for perpendicular and parallel polarization at lower and higher energy ranges. On the contrary, FePS₃ exhibits a strong anisotropic trend for both perpendicular and parallel polarization with an increased number of peaks for dielectric constants at the given energy range. Moreover, the calculated frequency-dependent dielectric functions show a similar trend between 5 eV to 40 eV and 60 eV to 100 eV with increased number peaks of FePS₃ for both perpendicular and parallel polarization as compared to MnPS₃, which clearly demonstrates the effect of isotropic and anisotropic trend on MnPS₃ and FePS₃, respectively.

Table 2. Total energy calculations for ferromagnetic (FM) and anti-ferromagnetic (AFM) state and their difference for MnPS₃ and FePS₃.

Materials	E ₀ (FM Calculation)	E ₀ (AFM Calculation)	dE ₀ (FM-AFM)
MnPS ₃	114.92800 eV	114.32689 eV	0.601 eV
FePS ₃	164.99485 eV	163.97464 eV	1.02 eV

4. Conclusions

High-quality single crystals of MnPS₃ and FePS₃ were synthesized by using CVT. The EPR and VSM were used to corroborate the existence of antiferromagnetic behavior and to study isotropy/anisotropy in these materials. The probe for the magnetic character of MnPS₃ and FePS₃ was carried out at 120 K, 200 K and 300 K. The susceptibility showed a typical antiferromagnetic behavior in MnPS₃ with an isotropic trend, while an anisotropic behavior was witnessed for FePS₃. Moreover, our calculations further confirmed that the antiferromagnetic state was additionally stable than the ferromagnetic state for both MnPS₃ and FePS₃. The projected density of states (PDOS) manifested a vital irregularity between spin-up and spin-down channels of Mn and Fe 3d states, which is responsible for the primary contribution to the antiferromagnetic states near the Fermi level. The frequency-dependent dielectric function calculations have shown that MnPS₃ possessed strong isotropic behavior for both perpendicular polarization and parallel polarization at lower and higher energy ranges. On the contrary, FePS₃ exhibited strong anisotropic trend for both perpendicular as well as for parallel polarizations at the given energy range.

Author Contributions: L.S. conceived and designed the experiments; Z.u.R. performed the experiments and analyzed the data; Z.M. performed the computational study, O.A.M, C.W. and Q.H helped in analysis of the data; W.Z. contributed in providing analysis tools; M.H. provided help in writing the paper.

Acknowledgments: This work is partially supported by MOST (2017YFA0303500, 2014CB848900), NSFC (U1532112, 11574280), CAS Key Research Program of Frontier Sciences (QYZDB-SSW-SLH018) and CAS Interdisciplinary Innovation Team. Z.R., Z.M., O.A.M. and M.H. thank CSC fellowship. We would like to thank the Hefei Synchrotron Radiation Facility (ARPES, Photoemission and MCD End stations) and the USTC Center for Micro and Nanoscale Research and Fabrication for help in characterizations.

Conflicts of Interest: The authors declare no conflict of interest.

References

- Zhu, J.; Yang, Y.; Jia, R.; Liang, Z.; Zhu, W.; Rehman, Z.U.; Bao, L.; Zhang, X.; Cai, Y.; Song, L.; et al. Ion Gated Synaptic Transistors Based on 2D van der Waals Crystals with Tunable Diffusive Dynamics. *Adv. Mater.* **2018**, *30*. [[CrossRef](#)] [[PubMed](#)]
- Brec, R. Review on structural and chemical properties of transition metal phosphorous trisulfides MPS₃. *Solid State Ion.* **1986**, *22*, 3–30. [[CrossRef](#)]
- Tian, Y.; Gray, M.J.; Ji, H.; Cava, R.; Burch, K.S. Magneto Elastic Coupling in A Potential Ferromagnetic 2D Atomic Crystal. *2D Mater.* **2016**, *3*. [[CrossRef](#)]

4. Nicolosi, V.; Chhowalla, M.; Kanatzidis, M.G.; Strano, M.S.; Coleman, J.N. Liquid Exfoliation of Layered Materials. *Science* **2013**, *340*. [[CrossRef](#)]
5. Long, G.; Zhang, T.; Cai, X.; Hu, J.; Cho, C.-W.; Xu, S.; Shen, J.; Wu, Z.; Han, T.; Lin, J.; et al. Isolation and Characterization of Few-Layer Manganese Thiophosphite. *ACS Nano* **2017**, *11*, 11330–11336. [[CrossRef](#)] [[PubMed](#)]
6. Zhang, X.; Zhao, X.; Wu, D.; Jing, Y.; Zhou, Z. MnPSe₃ Monolayer: A Promising 2D Visible-Light Photohydrolytic Catalyst with High Carrier Mobility. *Adv. Sci.* **2016**, *3*. [[CrossRef](#)] [[PubMed](#)]
7. Lee, J.-U.; Lee, S.; Ryoo, J.H.; Kang, S.; Kim, T.Y.; Kim, P.; Park, C.-H.; Park, J.-G.; Cheong, H. Ising-Type Magnetic Ordering in Atomically Thin FePS₃. *Nano Lett.* **2016**, *16*, 7433–7438. [[CrossRef](#)] [[PubMed](#)]
8. Du, K.-Z.; Wang, X.-Z.; Liu, Y.; Hu, P.; Utama, M.I.B.; Gan, C.K.; Xiong, Q.; Kloc, C. Weak Van der Waals stacking, Wide-Range Band Gap, and Raman Study on Ultrathin Layers of Metal Phosphorus Trichalcogenides. *ACS Nano* **2016**, *10*, 1738–1743. [[CrossRef](#)] [[PubMed](#)]
9. Wang, X.; Du, K.; Liu, Y.Y.F.; Hu, P.; Zhang, J.; Zhang, Q.; Owen, M.H.S.; Lu, X.; Gan, C.K.; Sengupta, P. Raman Spectroscopy of Atomically Thin Two-Dimensional Magnetic Iron Phosphorus Trisulfide (FePS₃) Crystals. *2D Mater.* **2016**, *3*. [[CrossRef](#)]
10. Chatterjee, I. Magnetic properties of layered antiferromagnets. *Phys. Rev. B* **1995**, *51*, 3937–3940. [[CrossRef](#)]
11. De Groot, R.; Mueller, F.M.; van Engen, P.G.; Buschow, K.H.J. New class of materials: Half-metallic ferromagnets. *Phys. Rev. Lett.* **1983**, *50*. [[CrossRef](#)]
12. Brataas, A.; Hals, K.M.D. Spin-orbit torques in action. *Nat. Nanotechnol.* **2014**, *9*, 86–88. [[CrossRef](#)] [[PubMed](#)]
13. Wadley, P.; Howells, B.; Železný, J.; Andrews, C.; Hills, V.; Champion, R.P.; Novák, V.; Olejník, K.; Maccherozzi, F.; Dhesi, S.S. Electrical switching of an antiferromagnet. *Science* **2016**, *351*, 587–590. [[CrossRef](#)] [[PubMed](#)]
14. Jungwirth, T.; Marti, X.; Wadley, P.; Wunderlich, J. Antiferromagnetic spintronics. *Nat. Nanotechnol.* **2016**, *11*, 231–241. [[CrossRef](#)] [[PubMed](#)]
15. Van den Brink, A.; Vermijs, G.; Solognac, A.; Koo, J.; Kohlhepp, J.T.; Swagten, H.J.M.; Koopmans, B. Field-free magnetization reversal by spin-Hall effect and exchange bias. *Nat. Commun.* **2016**, *7*. [[CrossRef](#)] [[PubMed](#)]
16. Taniguchi, H.; Suzuki, S.; Arakawa, T.; Yoshida, H.; Niimi, Y.; Kobayashi, K. Fabrication of thin films of two-dimensional triangular antiferromagnet Ag₂CrO₂ and their transport properties. *AIP Adv.* **2018**, *8*. [[CrossRef](#)]
17. Joy, P.; Vasudevan, S. Magnetism in the layered transition-metal thiophosphates MPS₃ (M = Mn, Fe, and Ni). *Phys. Rev. B* **1992**, *46*. [[CrossRef](#)]
18. Wei, X.; Yan, F.; Shen, C.; Lv, Q.; Wang, K. Photodetectors based on junctions of two-dimensional transition metal dichalcogenides. *Chin. Phys. B* **2017**, *26*. [[CrossRef](#)]
19. Li, X.; Cao, T.; Niu, Q.; Shi, J.; Feng, J. Coupling the valley degree of freedom to antiferromagnetic order. *Proc. Nat. Acad. Sci. USA* **2013**, *110*, 3738–3742. [[CrossRef](#)] [[PubMed](#)]
20. Lagadic, I.; Lacroix, P.G.; Clément, R. Layered MPS₃ (M = Mn, Cd) thin films as host matrixes for nonlinear optical material processing. *Chem. Mater.* **1997**, *9*, 2004–2012. [[CrossRef](#)]
21. Grasso, V. Low-dimensional materials: The MPX₃. In *NuovoCimentoRivistaSerie*; EditriceCompositori: Bologna, Italy, 2002.
22. Wildes, A.; Rønnow, H.M.; Roessli, B.; Harris, M.J.; Godfrey, K.W. Anisotropy and the critical behaviour of the quasi-2D antiferromagnet, MnPS₃. *J. Magn. Magn. Mater.* **2007**, *310*, 1221–1223. [[CrossRef](#)]
23. Wildes, A.; Ronnow, H.M.; Roessil, B.; Harris, M.J.; Godfrey, K.W. Static and dynamic critical properties of the quasi-two-dimensional antiferromagnet MnPS₃. *Phys. Rev. B* **2006**, *74*. [[CrossRef](#)]
24. Kuo, C.-T.; Neumann, M.; Balamurugan, K.; Ju Park, H.; Kang, S.; Shiu, H.W.; Kang, J.H.; Hong, B.H.; Han, M.; Won Noh, T.; et al. Exfoliation and Raman spectroscopic fingerprint of few-layer NiPS₃ van der Waals crystals. *Sci. Rep.* **2016**, *6*. [[CrossRef](#)] [[PubMed](#)]
25. Nesbitt, H.; Banerjee, D. Interpretation of XPS Mn (2p) spectra of Mn oxyhydroxides and constraints on the mechanism of MnO₂ precipitation. *Am. Mineral.* **1998**, *83*, 305–315. [[CrossRef](#)]
26. Jagličić, Z.; Mazej, Z. Antiferromagnetic CsCrF₅ and canted antiferromagnetism in RbCrF₅ and KCrF₅. *J. Magn. Magn. Mater.* **2017**, *434*, 112–117. [[CrossRef](#)]
27. Yamashita, T.; Hayes, P. Analysis of XPS spectra of Fe²⁺ and Fe³⁺ ions in oxide materials. *Appl. Surf. Sci.* **2008**, *254*, 2441–2449. [[CrossRef](#)]

28. Wang, M.; Zeng, L.; Chen, Q. Controlled synthesis of Co₃O₄ nanocubes under external magnetic fields and their magnetic properties. *Dalton Trans.* **2011**, *40*, 597–601. [[CrossRef](#)] [[PubMed](#)]
29. Mørup, S.; Madsen, D.E.; Frandsen, C.; Bahl, C.R.H.; Hansen, M.F. Experimental and theoretical studies of nanoparticles of antiferromagnetic materials. *J. Phys. Condens. Matter* **2007**, *19*. [[CrossRef](#)]
30. Ewing, G. *Analytical Handbook Instrumentation*; Marcel Dekker: New York, NY, USA, 1997.
31. Heczko, O.; Straka, L.; Lanska, N.; Ullakko, K.; Enkovaara, J. Temperature dependence of magnetic anisotropy in Ni-Mn-Ga alloys exhibiting giant field-induced strain. *J. Appl. Phys.* **2002**, *91*, 8228–8230. [[CrossRef](#)]
32. Ma, Y.W.; Yi, J.B.; Ding, J.; Van, L.H.; Zhang, H.T.; Ng, C.M. Inducing ferromagnetism in ZnO through doping of nonmagnetic elements. *Appl. Phys. Lett.* **2008**, *93*. [[CrossRef](#)]
33. Thang, X. *Electron Paramagnetic Resonance Studies of Point Defects in AlGaN and SiC*; Linköping University Electronic Press: Linköping, Sweden, 2015; Volume 1670.
34. Kresse, G.; Furthmüller, J. Efficient iterative schemes for ab initio total-energy calculations using a plane-wave basis set. *Phys. Rev. B Condens. Matter* **1996**, *54*, 11169–11186. [[CrossRef](#)] [[PubMed](#)]
35. Blochl, P.E. Projector augmented-wave method. *Phys. Rev. B Condens. Matter* **1994**, *50*, 17953–17979. [[CrossRef](#)] [[PubMed](#)]
36. Kresse, G.; Joubert, D. From ultrasoft pseudopotentials to the projector augmented-wave method. *Phys. Rev. B* **1999**, *59*, 1758–1775. [[CrossRef](#)]
37. Perdew, J.P.; Burke, K.; Ernzerhof, F. Generalized gradient approximation made simple. *Phys. Rev. Lett.* **1996**, *77*, 3865–3868. [[CrossRef](#)] [[PubMed](#)]
38. Monkhorst, H.J.; Pack, J.D. Special points for Brillouin-zone integrations. *Phys. Rev. B* **1976**, *13*. [[CrossRef](#)]
39. Da Silva, J.L.; Ganduglia-Pirovano, M.V.; Sauer, J.; Bayer, V.; Kresse, G. Hybrid functionals applied to rare-earth oxides: The example of ceria. *Phys. Rev. B* **2007**, *75*. [[CrossRef](#)]
40. Wen, X.-D.; Martin, R.L.; Roy, L.E.; Scuseria, G.E.; Rudin, S.P.; Batista, E.R.; McCleskey, T.M.; Scott, B.L.; Bauer, E.; Joyce, J.J.; et al. Effect of spin-orbit coupling on the actinide dioxides AnO₂ (An = Th, Pa, U, Np, Pu, and Am): A screened hybrid density functional study. *J. Chem. Phys.* **2012**, *137*. [[CrossRef](#)] [[PubMed](#)]



© 2018 by the authors. Licensee MDPI, Basel, Switzerland. This article is an open access article distributed under the terms and conditions of the Creative Commons Attribution (CC BY) license (<http://creativecommons.org/licenses/by/4.0/>).